Synthesis, Crystal Structure, and Magnetic Properties of $Sr_{1.31}Co_{0.63}Mn_{0.37}O_3$: A Derivative of the Incommensurate Composite Hexagonal Perovskite Structure

Tapas Kumar Mandal,[†] Artem M. Abakumov,[‡] Joke Hadermann,[§] Gustaaf Van Tendeloo,[§] Mark Croft,[⊥] and Martha Greenblatt*[,†]

Department of Chemistry and Chemical Biology, Rutgers, The State University of New Jersey, 610 Taylor Road, Piscataway, New Jersey 08854; Department of Chemistry, Moscow State University, Moscow 119991, Russia; Electron Microscopy for Materials Research (EMAT), University of Antwerp, Groenenborgerlaan 171, B-2020, Antwerp, Belgium; and Department of Physics and Astronomy, Rutgers, The State University of New Jersey, 136 Frelinghuysen Road, Piscataway, New Jersey 08854

Received July 12, 2007. Revised Manuscript Received September 24, 2007

We report the synthesis, structural investigation, and magnetic property studies of $Sr_{1.31}Co_{0.63}Mn_{0.37}O_3$ that adopts an incommensurate composite hexagonal perovskite-related structure. The crystal structure has been solved using a (3 + 1)-dimensional superspace approach from powder X-ray and neutron diffraction data (SSG $R\bar{3}m(00\gamma)0s$, $a = 9.5548(1)$ Å, $c = 2.5599(1)$ Å, $\mathbf{q} = 0.65581(4)\mathbf{c}^*$, $R_B = 0.041$, $R_P = 0.059$). The structure consists of face-sharing chains of octahedra and trigonal prisms, wherein the trigonal prismatic sites are preferentially occupied by Co with some cation disorder. A combination of electron diffraction and high-resolution electron microscopic analysis has demonstrated that the compound possesses a complicated microstructure related to the formation of domains with slightly different lengths of the modulation vector. X-ray absorption near-edge spectroscopic (XAS) studies clearly indicate the presence of Mn in the 4+ and Co in the 3+ oxidation state. While the magnetic susceptibility data indicates the presence of antiferromagnetic correlations in the system, the calculation of effective paramagnetic moment ($\mu_{cal} = 3.561\ \mu_B$), assuming the metal oxidation states as obtained from XAS and the cation distribution as obtained from neutron refinement, is in agreement with the value obtained experimentally ($\mu_{exp} = 3.676\ \mu_B$).

1. Introduction

Recently, a considerable amount of research effort has been devoted to elucidate the crystal structure of a class of 2H-hexagonal perovskite-related compounds using a superspace formalism[1–9] in (3 + 1)-dimensional [(3 + 1)D] space, especially in cases where the structure is incommensurately modulated. The key structural feature being the presence of one-dimensional (1D) chains of transition metal–oxygen polyhedra, their unique low-dimensional (LD) magnetic properties are of immense interest.[10–23] Thus, the family of oxides generically represented by the $A_{3n+3m}A'_nB_{3m+n}O_{9m+6n}$ (where n and m are the number of $A_3A'O_6$ and A_3O_9 layers, respectively) formula, closely related to the 2H-hexagonal perovskites became important, although in 1995 Darriet and

* To whom correspondence should be addressed: e-mail martha@rutchem.rutgers.edu; Tel (732) 445 3277; Fax (732) 445 5312.
[†] Department of Chemistry and Chemical Biology, Rutgers, The State University of New Jersey.
[‡] Moscow State University.
[§] University of Antwerp.
[⊥] Department of Physics and Astronomy, Rutgers, The State University of New Jersey.

(1) Evain, M.; Boucher, F.; Gourdon, O.; Petricek, V.; Dusek, M.; Bezdicka, P. *Chem. Mater.* **1998**, *10*, 3068.
(2) Gourdon, O.; Petricek, V.; Dusek, M.; Bezdicka, P.; Durovic, S.; Gyepesova, D.; Evain, M. *Acta Crystallogr.* **1999**, *B55*, 841.
(3) Perez-Mato, J. M.; Zakhour-Nakhl, M.; Weill, F.; Darriet, J. *J. Mater. Chem.* **1999**, *9*, 2795.
(4) Zakhour-Nakhl, M.; Claridge, J. B.; Darriet, J.; Weill, F.; zur Loye, H.-C.; Perez-Mato, J. M. *J. Am. Chem. Soc.* **2000**, *122*, 1618.
(5) Zakhour-Nakhl, M.; Weill, F.; Darriet, J.; Perez-Mato, J. M. *Int. J. Inorg. Mater.* **2000**, *2*, 71.
(6) Zakhour-Nakhl, M.; Darriet, J.; Claridge, J. B.; zur Loye, H.-C.; Perez-Mato, J. M. *Int. J. Inorg. Mater.* **2000**, *2*, 503.
(7) Stitzer, K. E.; El Abed, A.; Darriet, J.; zur Loye, H.-C. *J. Am. Chem. Soc.* **2001**, *123*, 8790.
(8) Stitzer, K. E.; Darriet, J.; zur Loye, H.-C. *Curr. Opin. Solid State Mater. Sci.* **2001**, *5*, 535.
(9) El Abed, A.; Gaudin, E.; zur Loye, H.-C.; Darriet, J. *Solid State Sci.* **2003**, *5*, 59.
(10) Nguyen, T. N.; Giaquinta, D. M.; zur Loye, H.-C. *Chem. Mater.* **1994**, *6*, 1642.
(11) Nguyen, T. N.; zur Loye, H.-C. *J. Solid State Chem.* **1995**, *117*, 300.
(12) Vente, J. F.; Lear, J. K.; Battle, P. D. *J. Mater. Chem.* **1995**, *5*, 1785.
(13) Nguyen, T. N.; Lee, P. A.; zur Loye, H.-C. *Science* **1996**, *271*, 489.
(14) Darriet, J.; Grasset, F.; Battle, P. D. *Mater. Res. Bull.* **1997**, *32*, 139.
(15) Kageyama, H.; Yoshimura, K.; Kosuge, K.; Mitamura, H.; Goto, T. *J. Phys. Soc. Jpn.* **1997**, *66*, 1607.
(16) Kageyama, H.; Yoshimura, K.; Kosuge, K. *J. Solid State Chem.* **1998**, *140*, 14.
(17) Kawasaki, S.; Takano, M.; Inami, T. *J. Solid State Chem.* **1999**, *145*, 302.
(18) Niitaka, S.; Kageyama, H.; Kato, M.; Yoshimura, K; Kosuge, K. *J. Solid State Chem.* **1999**, *146*, 137.
(19) Irons, S. H.; Sangrey, T. D.; Beauchamp, K. M.; Smith, M. D.; zur Loye, H.-C. *Phys. Rev. B* **2000**, *61*, 11594.
(20) zur Loye, H.-C.; Stitzer, K. E.; Smith, M. D.; El Abed, A.; Darriet, J. *Inorg. Chem.* **2001**, *40*, 5152.
(21) Zubkov, V. G.; Bazuev, G. V.; Tutyunnik, A. P.; Berger, I. F. *J. Solid State Chem.* **2001**, *160*, 293.
(22) El Abed, A.; Gaudin, E.; Lemaux, S.; Darriet, J. *Solid State Sci.* **2001**, *3*, 887.
(23) El Abed, A.; Gaudin, E.; Darriet, J.; Whangbo, M.-H. *J. Solid State Chem.* **2002**, *163*, 513.

10.1021/cm071840g CCC: $37.00
Published on Web 11/13/2007

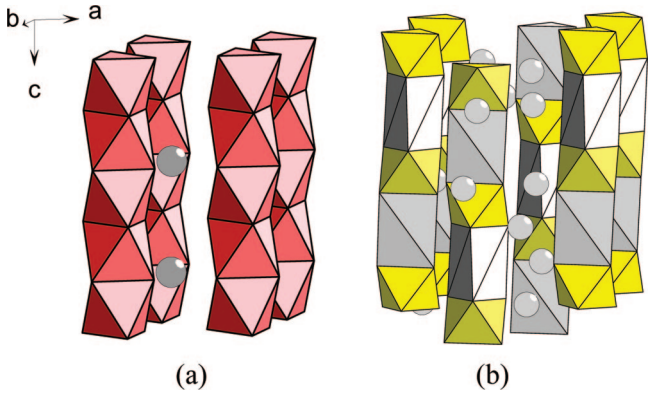

Figure 1. Structure of (a) 2H-hexagonal perovskite and (b) Sr_4PtO_6.

Subramanian[24] recognized the existence of such a series for the first time. They not only established the basic feature of their crystal structure by a mixed stacking of A_3O_9 and $A_3A'O_6$ layers and their close relationship to that of 2H-hexagonal perovskites but also predicted other new members of the series that were realized later on.[1,25–28] It is well-known that the 2H-hexagonal perovskite structure can be considered as hexagonal close-packed stacking of the AO_3 layers with transition metal cations in the octahedral holes created in between the layers giving the composition ABO_3. The conventional AO_3 layer is often described more conveniently as an A_3O_9 layer. It has also been recognized that the $A_3A'O_6$ layer can be generated by an ordered removal of three oxygen atoms from an A_3O_9 layer and subsequently replacing it by an A′ cation in the newly created trigonal prismatic site.[24] In a simple way, numerous compositions can be derived by a mixed stacking of *m*-A_3O_9 and *n*-$A_3A'O_6$ layers with the general formula $A_{3n+3m}A'_nB_{3m+n}O_{9m+6n}$, where the B metal atom occupies the octahedral holes in between the layers. The two end members of this series correspond to the 2H ABO_3 ($n = 0$; $m = 1$) perovskite (e.g., $BaNiO_3$)[29] and the Sr_4PtO_6[30] ($n = 1$; $m = 0$) structure. While the 2H structure (Figure 1a) contains parallel chains of all face-shared octahedra, the Sr_4PtO_6 structure (Figure 1b) comprises face-shared chains of alternating octahedra and trigonal prisms, the same as that of the K_4CdCl_6 structure type.[31] In between these two compositions, an unlimited number of closely related structures can be envisaged by merely varying the ratio of the octahedra and trigonal prisms.

In the superspace approach this variety of structures can be explained by a unique composite structure model.[1,3] The composite structure is considered to be composed of two mutually interacting subsystems ($[(A',B)O_3]_\infty$ and $[A]_\infty$ chains) that have common periodicity in the *a–b* plane (common *a, b* parameters) but different repeat periods along *c* (different *c* parameters). An interaction between the subsystems results in their mutual modulations. The general composition of this family is better formulated in an equivalent way as $A_{1+x}(A'_xB_{1-x})O_3$, where $x = n/(3m + 2n)$ and depends on the ratio of c_1 (the *c*-lattice parameter of subsystem 1) to c_2 (the *c*-lattice parameter of subsystem 2) giving rise to a modulation vector $\mathbf{q} = \gamma\mathbf{c}_1^*$ with $\gamma = c_1/c_2 = (1 + x)/2$. The structure is commensurately modulated for rational γ values. However, if γ cannot be approximated by a rational number with a reasonably small denominator, the structure is better considered as incommensurately modulated.

Depending on the number of unpaired d-electrons on the transition metal ions, as well as the exact sequence of octahedra and trigonal prisms in the chains, various magnetic exchange pathways may be present in the $A_{3n+3m}A'_nB_{3m+n}O_{9m+6n}$ system. As a result, multiple exchange interactions of different strengths within the chains and in between the chains can give rise to diverse magnetic properties that include antiferromagnetism, ferromagnetism, and a combination of both, often complicating the interpretation of the magnetic data. Among several systems, the magnetism of the $n = \infty$ member ($A_3A'BO_6$) has been extensively investigated,[10–19,21] particularly to model 1D electronic behavior.[10–13] Nevertheless, it is counter argued that such systems cannot be considered purely 1D with a number of compounds that show 3D magnetic ordering.[14,19] For example, in Ca_3NaRuO_6,[14] a long-range antiferromagnetic order was evidenced by the maximum in the magnetic susceptibility data below 90 K. Similarly, $Sr_3CuPt_xIr_{1-x}O_6$ cannot be simply described as a 1D quantum spin chain with competing ferromagnetic and antiferromagnetic interactions.[19] A ferrimagnetic coupling of ferromagnetic chains has been suggested for $Ca_3Co_2O_6$.[15]

The magnetic properties of the $n \neq \infty$ compositions show more complex behavior. The plateau observed in the magnetic susceptibility data for $Sr_4Mn_2NiO_9$[22] is attributed to antiferromagnetically coupled spin dimers and paramagnetic Ni^{2+} ions while the interaction between the two is weak. The magnetic transition observed at ~3 K is attributed to the 3D magnetic ordering. El Abed et al.[23] have carried out spin dimer analysis of the Mn^{4+} ion sublattice in the system $Sr_{1+x}Mn_{1-x}Ni_xO_3$ ($x = 1/3$ and 0.324) to determine the relative strengths of spin-exchange interactions. Their analysis identified weakly interacting antiferromagnetically coupled $(Mn^{4+})_2$ dimers and an Ni^{2+} ion sublattice that are nearly independent. In $Sr_4Mn_2ZnO_9$,[32] the presence of pronounced antiferromagnetic character with a broad susceptibility maximum at 100 K has been attributed to short-range ordering. At low temperatures, the susceptibility data showed a transition to a 3D long-range ordered state. A similar study by Moore et al.[33] also suggested adoption of an antiferromagnetic structure at low temperatures. Last but

(24) Darriet, J.; Subramanian, M. A. *J. Mater. Chem.* **1995**, *5*, 543.
(25) Campa, J.; Gutierrez-Puebla, E.; Monge, A.; Rasines, I.; Ruiz-Valero, C. *J. Solid State Chem.* **1996**, *126*, 27.
(26) Blake, G. R.; Sloan, J.; Vente, J. F.; Battle, P. D. *Chem. Mater.* **1998**, *10*, 3536.
(27) Claridge, J. B.; zur Loye, H.-C. *Mater. Res. Soc. Symp. Proc.* **1999**, 547.
(28) Jordan, N. A.; Battle, P. D.; van Smaalen, S.; Wunschel, M. *Chem. Mater.* **2003**, *15*, 4262.
(29) Lander, J. J. *Acta Crystallogr.* **1951**, *4*, 148.
(30) Randall, J. J.; Katz, L. *Acta Crystallogr.* **1959**, *12*, 519.
(31) Bergerhoff, G.; Schmitz-Dumont, O. *Z. Anorg. Allg. Chem.* **1956**, *284*, 10.
(32) Hernando, M.; Boulahya, K.; Parras, M.; Gonzáales-Calbet, J. M. *Eur. J. Inorg. Chem.* **2002**, *2002*, 3190.
(33) Moore, C. A.; Battle, P. D. *J. Solid State Chem.* **2003**, *176*, 88.

not least, a partially ordered antiferromagnetic state has been observed in $Sr_{3.3}Ca_{0.7}CoRh_2O_9$.[34]

In light of the foregoing, we describe herein the synthesis, crystal, and magnetic structure of a derivative of the $A_{3n+3m}A'_nB_{3m+n}O_{9m+6n}$ family of oxides of nominal composition $Sr_{1.31}Co_{0.63}Mn_{0.37}O_3$. The $Sr_4Co_{3-x}Mn_xO_9$ ($0.5 \leq x \leq 2$) solid solutions and their magnetic properties have recently been described; however, the crystal structure was not yet solved.[35] Using a combination of electron diffraction, high-resolution electron microscopy, and superspace analysis of both the X-ray and neutron powder diffraction data, we have demonstrated that the compounds in this system possess a complicated microstructure related to the formation of domains in which there are slightly different lengths of the modulation vector. The distribution of Co and Mn over the octahedral and trigonal prismatic sites has been evaluated with the help of neutron diffraction. X-ray absorption near-edge spectroscopy (XAS) study clearly indicated the presence of Mn in the 4+ and Co in the 3+ oxidation states unlike other similar systems recently investigated where both 3+/2+ oxidation state for Co and 4+/2+ oxidation state for Mn are prevalent[21,28] and in contrast to the 4+/2+ oxidation state for Co and 4+ oxidation state for Mn proposed by Melkozerova and Bazuev.[35]

2. Experimental Section

The sample of nominal composition $Sr_{1.3}Co_{0.64}Mn_{0.36}O_3$ was prepared by the ceramic route. Stoichiometric quantities of high-purity SrO_2, Co_3O_4, and Mn_2O_3 were ground thoroughly inside an Ar-filled dry glovebox, and the resulting mixture was reacted in an alumina boat at 850, 900, 950, and 1000 °C for 24 h each in air with a final annealing step at 1050 °C for 24 h under oxygen flow and slow cooling of the reaction product. The reaction mixture was thoroughly ground in every intermediate step between each heating cycle. The same composition was also prepared by a solution-based route, namely, the citrate route, to ensure a more homogeneous mixing of the reactants. For this purpose, stoichiometric quantities of high-purity $SrCO_3$, $MnC_2O_4 \cdot 2H_2O$, and Co metal powders were dissolved in warm dilute nitric acid and heated gently until a clear solution was obtained. To this, citric acid was added, and the solution was slowly evaporated to a voluminous solid residue which was then calcined in a porcelain crucible at 400 and 600 °C for about 4 h each to remove organic matters. Then, the black powder was heat treated at 900 °C for 48 h and 925 °C for 72 h followed by a final oxygen anneal at 1050 °C for 48 h with thorough intermittent grindings.

Powder X-ray diffraction (PXD) patterns were recorded in Bragg–Brentano geometry using Cu Kα radiation with a Bruker D8-Advance diffractometer and a SOL-X solid-state detector. For Rietveld refinement, the PXD data were recorded in the 2θ range 15–120° in steps of 0.02° and with a step time of 9 s. Neutron powder diffraction (NPD) data were collected with the high-resolution BT-1 32 detector neutron powder diffractometer at the NIST Center for Neutron Research (NCNR), NBSR. A Cu(311) monochromator with a 90° takeoff angle, $\lambda = 1.5403(2)$ Å, and in-pile collimation of 15 min of arc were used. Data were collected over the range of 3–168° 2θ with a step size of 0.05°. The instrument is described in the NCNR WWW site (http://www.ncnr.nist.gov/).

Rietveld refinement of both the PXD and NPD was carried out with the JANA2000 program.[36]

Electron diffraction (ED) studies were performed with a Phillips CM20 microscope and high-resolution electron microscopy (HREM) with a JEOL 4000EX instrument. Energy-dispersive X-ray (EDX) spectra were obtained on the Phillips CM20 with an Oxford INCA system. The HREM images were simulated by means of the MacTempas software.

Magnetic measurements were performed with a Quantum Design MPMS-XL superconducting quantum interference device (SQUID) magnetometer. Temperature-dependent susceptibilities were measured at various applied magnetic fields up to 5 T in the temperature range $5 < T$ (K) < 400 after cooling the sample in zero magnetic field (zero field cooled, ZFC) and also while cooling in presence of the field (field cooled, FC). Measurements of magnetization (M) as a function of field (H) were made at 5 and 300 K over the magnetic field range $-50 \leq H$ (kOe) ≤ 50.

The Co and Mn–K XAS measurements were performed in the fluorescence mode on powdered samples on beam line X-19A at the Brookhaven National Synchrotron Light Source with methods discussed in refs 37 and 38. Briefly, the procedure that was used is the following. The incident and transmitted beam intensities were measured with ionization chambers and the fluorescence intensities with Canberra PIPS detectors. The absolute energy calibration was set to the elemental Co–K edge (first inflection point) 7.709 keV. The relative energy scale was maintained to better than ±0.05 eV with the simultaneously run standards. A similar procedure was followed while recording the data for the Mn–K edges as well. As is routinely done, the spectra had a linear background subtracted (determined over a ~80 eV interval below the edge) and were normalized to unity absorption step height across the edge. Here an average of the data in the ~50–200 eV range above the edge was used to set the normalization value.

3. Results and Discussion

3.1. Preliminary Characterization. The primary analysis of the PXD pattern of the $Sr_{1.3}Co_{0.64}Mn_{0.36}O_3$ sample prepared by a ceramic route revealed close similarity to the typical PXD patterns of the members of the $A_{3n+3m}A'_nB_{3m+n}O_{9m+6n}$ homologous series. Using an indexation scheme known for similar compounds,[39] the *hklm* indexes were assigned to the brightest reflections of both $[(Mn,Co)O_3]_\infty$ and $[Sr]_\infty$ subsystems, and the latttice parameters and the γ component of the modulation vector were determined as $a = 9.5531(3)$ Å, $c_1 = 2.5415(2)$ Å, and $\mathbf{q} = 0.64501(6)\mathbf{c}_1^*$. However, a closer inspection of the PXD pattern reveals extra fine features. Nonmonotonic variation of the reflection widths is present with sharp *hk*00 reflections (common for both subsystems) and much broader reflections with $l, m \neq 0$ (Figure 2). Such broadening behavior along with the shoulders at the low angle side for some of the reflections may indicate a local variation of the c parameter and/or modulation vector or a large amount of stacking faults in the material, which can be attributed to local inhomogeneity of the Co and Mn distribution.

(34) Hernando, M.; Boulahya, K.; Parras, M.; Varela, A.; Gonzáles-Calbet, J. M.; Martínez, J. L. *Chem. Mater.* **2002**, *14*, 4948.
(35) Melkozerova, M.; Bazuev, G. *Russ. J. Inorg. Chem.* **2006**, *51*, 362.
(36) Petricek, V.; Dusek, M. *The Crystallographic Computing System JANA2000*; Institute of Physics: Praha, Czech Republic, 2000.
(37) Tranquada, J. M.; Heald, S. M.; Moodenbaugh, A. R.; Liang, G.; Croft, M. *Nature (London)* **1989**, *337*, 720.
(38) Croft, M.; Sills, D.; Greenblatt, M.; Lee, C.; Cheong, S.-W.; Ramanujachary, K. V.; Tran, D. *Phys. Rev. B* **1997**, *55*, 8726.
(39) Mironov, A. V.; Abakumov, A. M.; Antipov, E. V. *Rigaku J.* **2003**, *19*, 23.

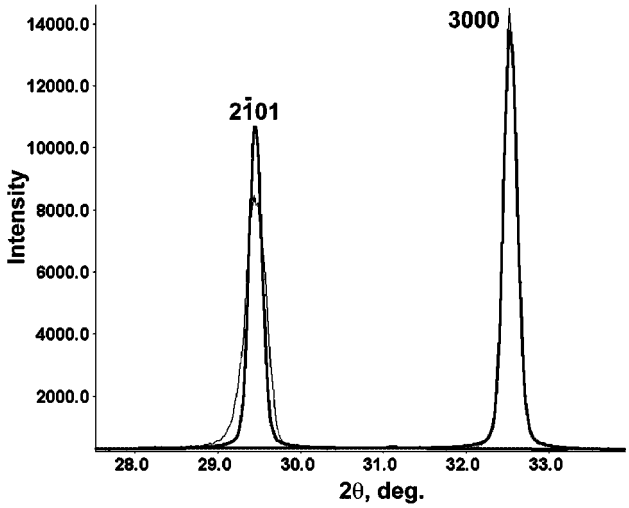

Figure 2. Part of the X-ray powder diffraction pattern for the ceramic $Sr_{1.3}Co_{0.64}Mn_{0.36}O_3$ sample illustrating different broadening of the *hk*00 reflections and reflections with $m \neq 0$. Experimental data are shown with thin line, and the thick line marks the profile fit with the full width at half-maximum parameters as for the 3000 reflection.

The $Sr_{1.3}Co_{0.64}Mn_{0.36}O_3$ sample prepared by a citrate route demonstrates significantly diminished anisotropic broadening of the reflections on the PXD pattern due to more homogeneous cation distribution. The preliminary Rietveld refinement from the PXD data for this sample was performed with a standard superspace model.[3] Because of the very close scattering factors of Co and Mn, no distinction can be made between these atoms with the PXD data. The final refinement resulted in reasonable values of the reliability factors for the main reflections and for satellites up to second order, confirming the proposed structure model (R_I(main reflections) = 0.038, R_I(first-order satellites) = 0.058, R_I(second-order satellites) = 0.064, R_P = 0.064).

3.2. Electron Diffraction and EDX Analysis. In order to shed light on the microstructure of the $Sr_{1.3}Co_{0.64}Mn_{0.36}O_3$ samples prepared using different techniques, a transmission electron microscopy investigation was undertaken. The ED patterns of $Sr_{1.3}Co_{0.64}Mn_{0.36}O_3$ (Figure 3a–c) can be indexed with the lattice parameters and modulation vector as determined from the PXD data. The extinction conditions correspond to the (3 + 1)D superspace group $R\bar{3}m(00\gamma)0s$, typical for this family of compounds. The detailed indexation scheme of similar ED patterns along with the description of the multiple diffraction and high order Laue zone effects is given by Abakumov et al.[40] Besides the ED patterns with well-defined diffraction spots, in the sample prepared via the ceramic route ED patterns were frequently observed (Figure 3d) where the *hk*00 reflections remain sharp, whereas the reflections with $l, m \neq 0$ become diffuse and elongated along the **c*** direction. This is attributed to a local variation of the γ component of the modulation vector and explains the anisotropic broadening and shoulders for the reflections on the PXD pattern.

The chemical composition of the grains in the ceramic sample should also vary locally in accordance with the

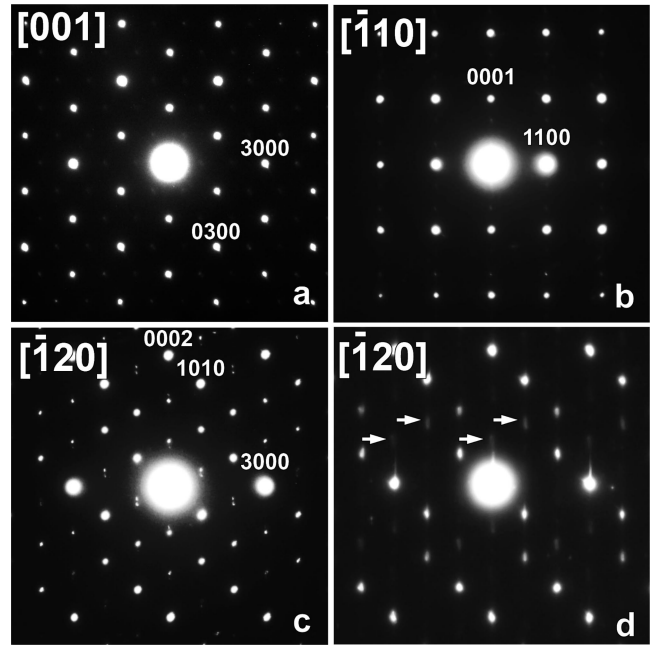

Figure 3. Electron diffraction patterns for $Sr_{1.3}Co_{0.64}Mn_{0.36}O_3$. Patterns with sharp satellite reflections (a–c) along with the pattern with diffuse satellites (d) are seen. The diffuse satellites are marked by arrows.

$A_{1+x}(A'_xB_{1-x})O_3$, $\gamma = (1 + x)/2$ formula. The cation composition $Sr_{1.33(3)}Co_{0.67(4)}Mn_{0.33(2)}$, measured by EDX analysis on the majority of the crystallites in the ceramic sample, is in good agreement with the bulk sample composition. However, crystallites were frequently found where the Co/Mn ratio deviates significantly from the bulk composition, exhibiting a Co content varying from 0.47(4):0.53(4) to 0.89(7):0.11(7). Variation of the Co/Mn ratio occurs even in the range of one crystallite, suggesting fragmentation into domains, which differ in composition and in length of the modulation vector. The Co/Mn ratio in the citrate sample was found to be uniform; the average cation composition of this sample corresponds to the formula $Sr_{1.42(15)}Co_{0.66(4)}Mn_{0.34(4)}$.

3.2. Rietveld Refinement from NPD Data. Because of the obviously better quality of the citrate $Sr_{1.3}Co_{0.64}Mn_{0.36}O_3$ sample, it was used for the refinement of the structure from NPD data. The NPD pattern taken at T = 5 K does not demonstrate any additional features compared to the NPD pattern taken at room temperature, indicating the absence of long-range magnetic ordering down to T = 5 K. Since slight chemical inhomogeneity remains, anisotropic strain broadening was taken into account using a method described by Stephens.[41] The superspace construction commonly applied for the $A_{3n+3m}A'_nB_{3m+n}O_{9m+6n}$ compounds was used.[1,3] The atomic displacements along the *c*-axis together with the occupational modulations were modeled with saw-tooth functions. Introducing harmonic displacement modulations for all atoms, except oxygen, with an orthogonalization procedure to reduce correlations does not improve the quality of the refinement, which means that no noticeable deviation from linear displacement occurs. Application of second-order harmonic positional modulations to the O atom reduces the

(40) Abakumov, A. M.; Mironov, A. V.; Govorov, V. A.; Lobanov, M. V.; Rozova, M. G.; Antipov, E. V.; Lebedev, O. I.; Van Tendeloo, G. *Solid State Sci.* **2003**, *5*, 1117.

(41) Stephens, P. W. *J. Appl. Crystallogr.* **1999**, *32*, 281.

Table 1. Selected Parameters from Rietveld Refinement of Neutron Powder Diffraction Data for $Sr_{1.31}Co_{0.63}Mn_{0.37}O_3$

formula	$Sr_{1.31}Co_{0.63}Mn_{0.37}O_3$
(3 + 1)D space group	$R\bar{3}m(00\gamma)0s$
a (Å)	9.5548(1)
c (Å)	2.5599(1)
q	0.65581(4)**c***
cell volume (Å^3)	202.40(1)
calculated density (g/cm^3)	5.422
temperature (K)	300
2θ range, step (deg)	$13 \le 2\theta \le 155$, 0.05
radiation, λ (Å)	1.5403
R_I(main reflections)	0.034
R_I(first-order satellites)	0.044
R_I(second-order satellites)	0.056
R_P, R_{wP}	0.059, 0.074
R_B	0.041

reliability factor from $R_{all} = 0.053$ to 0.041; this modulation was considered to be significant. The satellites up to second order were included into the refinement. For the A′ and B positions the isotropic atomic displacement parameters (ADPs) were fixed to $U_{iso} = 0.005$ Å^2, and the amount of Co and Mn in these positions was allowed to vary keeping these positions fully occupied. The occupancy factors of 0.08(4)Mn + 0.92(4)Co and 0.49(1)Mn + 0.51(1)Co were found for the A′ and B positions, respectively. It corresponds to the $Sr_{1.31}Co_{0.63}Mn_{0.37}O_3$ composition which is in excellent agreement with the bulk composition of the sample and the results of the EDX analysis. The refinement resulted in a satisfactory agreement between the experimental and calculated profiles ($R_P = 0.059$, $R_{wP} = 0.074$). The crystallographic data, atomic coordinates, and modulation parameters are summarized in Tables 1 and 2. The most relevant interatomic distances are listed in Table 3. Experimental, calculated, and difference NPD profiles are shown in Figure 4. Interatomic distances as a function of t coordinate are shown in Figures 5 and 6.

The refined value of the γ component of the modulation vector corresponds to the $x = 0.3116$ in the $A_{1+x}(A'_xB_{1-x})O_3$ formula which can be approximated as $p/q = 24/77$. The polyhedral chains then contain $p = 24$ trigonal prisms and $(q - p) = 53$ octahedra. Using the Farey tree, the p/q value can be expressed through the preceding "generators" p_1/q_1 and p_2/q_2 as $p/q = (p_1 + p_2)/(q_1 + q_2)$, giving rise to a complete sequence of polyhedra for the given rational p/q value.[3] Such analysis for $p/q = 24/77$ reveals the polyhedral sequence to be 4 × [1 × (3oct + 1prism) + 4 × (2oct + 1prism)] + 1 × [1 × (3oct + 1prism) + 3 × (2oct + 1prism)]. Thus, the $Sr_{1.31}Co_{0.63}Mn_{0.37}O_3$ structure is rather close to the idealized one with $x = 5/16$ ($\gamma = 21/32$) consisting of the blocks of 1 × (3oct + 1prism) + 4 × (2oct + 1prism) (Figure 7). This sequence in the real structure is periodically violated by the 1 × (3oct + 1prism) + 3 × (2oct + 1prism) blocks.

The crystal structure of similar compounds, but with significantly different Co/Mn ratio, $Sr_{1.266}Co_{0.266}Mn_{0.734}O_3$ and $Sr_{1.28}Co_{0.28}Mn_{0.72}O_3$, was reported earlier by Jordan et al.[28] It is assumed that in these compounds Co and Mn adopt valence states of 2+ and 4+, respectively. Mn^{4+} cations were found to occupy mainly the octahedral B site. Nevertheless, a significant part of the Mn^{4+} is located at the trigonal prismatic A′ site (up to 29% of the A′ site occupation), where the A′–O interatomic distances of 2.14–2.17 Å are too long for the Mn^{4+} cations. One can expect that, upon increasing the Co/Mn ratio, the Mn^{4+} cations should be replaced first at the A′ site, while the B site retains mixed occupation. Indeed, in the $Sr_{1.31}Co_{0.63}Mn_{0.37}O_3$ crystal structure the amount of Mn^{4+} at the A′ position is reduced to 8%, but the mixed occupancy still remains. In order to explain the unusually long A′–O interatomic distances, the off-center cation displacements toward one of two triangular faces were introduced in the $Ba_6Mn_4MO_{15}$ (M = Cu, Zn) oxides.[42] Such displacements split six equivalent A′–O distances into three shorter (1.98–2.10 Å) and three longer (2.39–2.55 Å) ones. However, attempts to refine the off-center A′ cation displacements for the $Sr_{1.31}Co_{0.63}Mn_{0.37}O_3$ crystal structure do not change significantly the x_3 coordinate of this position and do not decrease the reliability factors. One can assume that mixed cation occupancies can be caused by violation of perfect stacking sequences of the octahedra and trigonal prisms along the chains of the face sharing polyhedra (i.e., by stacking faults). Diffuse and elongated satellite reflections along **c***on the ED patterns (Figure 3) provide an indirect support for this assumption.

3.3. High-Resolution Electron Microscopy. To determine the domain structure, HREM images along the [$\bar{1}$20] zone were taken from the samples prepared by the citrate (Figure 8) and ceramic routes (Figure 9). Since the γ component of the modulation vector for the $Sr_{1.31}Co_{0.63}Mn_{0.37}O_3$ sample does not deviate significantly from the commensurate value of $\gamma = 2/3$, a commensurate approximation with the $Sr_4Co_2MnO_9$ composition, lattice parameters $a = 9.56$ Å, $c = 7.68$ Å, the $P321$ space group, and the atomic coordinates and Co/Mn distribution as determined from the NPD refinement were used for the calculation of the simulated HREM image (see square inset in the right part of Figure 8). The best agreement was found for a focus value $f = -850$ Å and a thickness $t = 50$ Å. At these imaging conditions, the rows of white dots correspond to the projections of the cation columns, with the Sr columns being projected in between each two bright dots in these rows. The bright dots in the thin part of the crystallite form a rectangular mesh corresponding to the primitive trigonal unit cell of the subsystem II. Because of the change in thickness on going from the edge of the crystallite to its center (from top to bottom of Figure 8), subsystem I becomes more prominent, and the positions of the bright dots in the central part of the image correspond to the R-centered trigonal unit cell of subsystem I. The unit cells of both subsystems are indicated on the enlarged part of the [$\bar{1}$20] image at the right side of Figure 8.

The modulations are visible in Figure 8 as diagonal dark stripes which are uniformly spaced and inclined with respect to the c-axis. The appearance of such stripes can be understood if one considers the bright dot contrast being caused by primary impact of the basic reflections of one of the subsystems. Then the reflections of the other subsystem form satellite arrays (shown by dashed lines on the Fourier

(42) Cussen, E. J.; Vente, J. F.; Battle, P. D. *J. Am. Chem. Soc.* **1999**, *121*, 3958.

Table 2. Structural Parameters Derived from the Refinement of Neutron Powder Diffraction Data for $Sr_{1.31}Co_{0.63}Mn_{0.37}O_3$[a]

atom	x_1	x_2	x_3	x_4	Δ	δ	U_{iso}, Å^2
			subsystem I: $R\bar{3}m(00\gamma)0s$				
A′	0	0	0	1/4	0.15581(4)	−0.0382	0.008(6)
0.08(4)Mn							
0.92(4)Co							
B	0	0	0	0	0.34419(4)	−0.0844	0.007(4)
0.49(1)Mn							
0.51(1)Co							
O	0.1553(2)	0.1553(2)	1/2	1/4	1/2	−0.123(1)	0.0110(4)
			subsystem II: $X-3c1(001/\gamma)$ (X = centering vectors (2/3, 1/3, 0, 1/3), (1/3, 2/3, 0, 2/3))				
Sr1	0.3230(8)	0	1/4	1/2	0.0959	−0.004(2)	0.012(3)
Sr2	0.3581(5)	0	1/4	0	0.2374	−0.010(5)	0.011(1)

[a] Harmonic modulation parameters and orthogonalization coefficients for the O site: $U_{x,2} = -U_{y,2} = -0.0012(2)$; $U_{x,3} = -U_{y,3} = -0.0043(2)$; $U_{z,3} = 0.006(1)$. Modulation function for the O site for the parameter λ is defined in a restricted interval as $U_\lambda(\bar{x}_4) \sum_{n=0}^{k} U_{\lambda,n}\mathrm{Ortho}_n(\bar{x}_4)$, where the orthogonalized functions obtained by a Shmidt orthogonalization routine, are given by $\mathrm{Ortho}_0(\bar{x}_4) = 1$; $\mathrm{Ortho}_1(\bar{x}_4) = -2.069 + 3.249\sin(2\pi\bar{x}_4)$; $\mathrm{Ortho}_2(\bar{x}_4) = 1.414\cos(2\pi\bar{x}_4)$; $\mathrm{Ortho}_3(\bar{x}_4) = -2.271\cos(2\pi\bar{x}_4) + 2.675\sin(4\pi\bar{x}_4)$.

Table 3. Refined Bond Distances from Powder Neutron Diffraction Data for $Sr_{1.31}Co_{0.63}Mn_{0.37}O_3$ (Å)

A′–O_{min}	2.087(8)
A′–O_{max}	2.124(11)
B–O_{min}	1.888(8)
B–O_{max}	1.920(6)
Sr1–O_{min}	2.634(7), 2.897(12), 2.502(12), 2.727(8), 2.724(8), 2.82(2) × 2, 2.632(7), 2.894(12), 2.501(14)
Sr3–O_{min}	2.626(12), 2.567(12), 2.671(10), 2.747(11), 2.389(13), 2.387(14), 2.623(11), 2.568(11)

transform in Figure 8), resulting in diagonally striped intensity modulations of the bright dots on the HREM image. Since the structure is treated as a composite one, the variation of the $c_1/c_2 = \gamma$ ratio (i.e., the length of the modulation vector, the ratio between octahedral and trigonal prismatic sites and, hence, the chemical composition) causes the stripes to change the inclination angle with respect to the *c*-axis. In the [$\bar{1}$20] HREM image of the ceramic sample the variation of the γ component of the modulation vector is visualized as a change in the angle between the normal to these stripes and the *c*-axis. This is clearly seen in Figure 9, demonstrating that the length of the modulation vector is different for the different encircled areas. These areas are present as small irregularly shaped domains within the same crystallite.

3.4. XAS Measurements. The near-edge features at the K edges of 3d row transition metal, T(3d), compounds are due to transitions from the 1s to 4p states of the transition metal. These features are superimposed on an underlying step feature due to the onset of 1s to continuum transitions. Multiple 4p features associated with different 3d configurations, and with differing orbital orientations, make interpretation of the near-edge features difficult. Nevertheless, the systematic energy shifts in the T(3d) K edges, upon doping/chemical changes, and the variation of feature intensities can serve as indicators of charge transfer.[43]

The Mn- and Co-K edges of the $Sr_{1.31}Co_{0.63}Mn_{0.37}O_3$ sample along with various standard compounds are shown in parts a and b of Figure 10, respectively. Figure 10a compares the Mn–K edge of $Sr_{1.31}Co_{0.63}Mn_{0.37}O_3$ to octahedrally coordinated standards, namely, $Mn^{2+}O$ with NaCl structure and perovskite-related $LaMn^{3+}O_3$ and $CaMn^{4+}O_3$. The systematic chemical shift to higher energy of the edge (near $\mu \sim 0.7$, for example) with increasing Mn valence and the constancy of the chemical shift of $Sr_{1.31}Co_{0.63}Mn_{0.37}O_3$ with that of the Mn^{4+} standard is clear (see oval in Figure 10a). The lack of a trigonal-prismatic Mn standard should not be crucial due to the strong octahedral site preference of Mn. Despite the near-edge structure variations expected from varying local symmetries, the chemical shift of $Sr_{1.31}Co_{0.63}Mn_{0.37}O_3$ appears highly consistent with the assignment of a Mn^{4+} valence state.

In Figure 10b the Co–K edge of $Sr_{1.31}Co_{0.63}Mn_{0.37}O_3$ sample is again compared with octahedrally coordinated standards comprised of a series of perovskite related compounds, namely, $La_2Co^{2+}O_4$, $LaCo^{3+}O_3$, $Sr_2Co^{3+}O_3Cl$, and $SrCo^{(4-2\delta)+}O_{3-\delta}$ along with $Co^{2+}O$ with the NaCl structure. The systematic chemical shift to higher energy of the edge (near $\mu \sim 0.7$, for example) with increasing Co valence and the constancy of the chemical shift of $Sr_{1.31}Co_{0.63}Mn_{0.37}O_3$ with those of the Co^{3+} standards is noteworthy (see oval in Figure 10b). Comparison of the chemical shift of $LaCoO_3$ to that of $Sr_{1.31}Co_{0.63}Mn_{0.37}O_3$ appears quite consistent with a Co^{3+} valence state assignment for the latter.

The Co–K edge spectrum of the $Sr_2Co^{3+}O_3Cl$ material, where one of the apical O is replaced by a Cl in the parent perovskite-related 214 compound, has been included in Figure 10b. The distorted local symmetry of the Co in this material leads to substantial splitting of the 4p states. This results in a broader Co–K edge with some spectral intensity being split up and down in energy precluding a simple comparison of the chemical shift to the octahedral compounds. This illustrates how such local structural changes can complicate valence estimation via the average chemical shift.

The weak pre-edge features at the K edges of T(3d) compounds are due to a combination of quadruple 1s to 3d and dipole 1s to 3d/ligand-p-hybridized transitions with the latter being dominant in oxide materials. The local symmetry of the ligand field strongly affects both the spectral strength and energy distribution of the features in the pre-edge region. Both the absence of appropriate trigonal-prismatic standards and the strongly mixed octahedral/trigonal-prismatic local symmetry in the compounds studied here makes clear valence state inferences based upon the pre-edge spectra nearly impossible.

(43) Qian, Q.; Tyson, T. A.; Kao, C. C.; Rueff, J. P.; de Groot, F. M. F.; Croft, M.; Cheong, S. W.; Greenblatt, M.; Subramanian, M. A. *J. Phys. Chem. Solids* **2000**, *61*, 457.

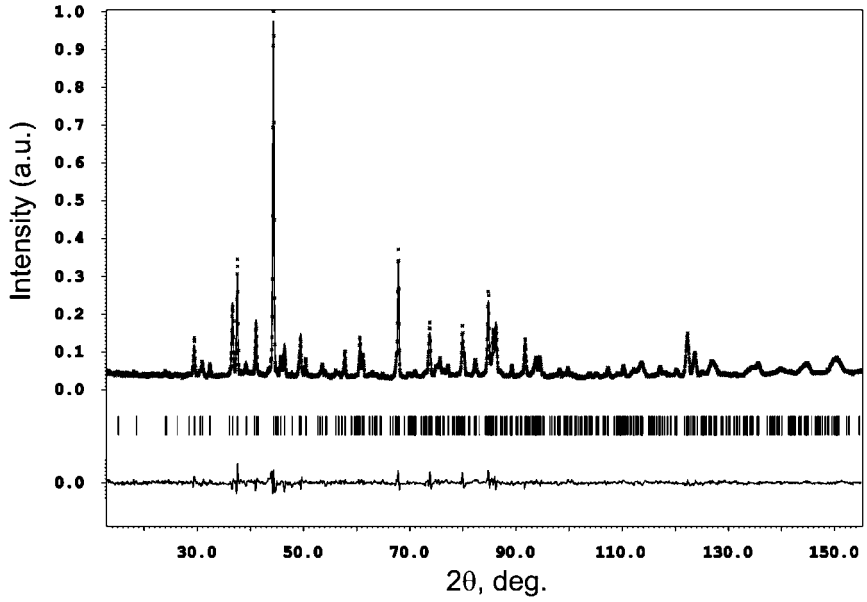

Figure 4. Observed (points), calculated (solid lines), and difference (bottom) neutron powder diffraction profiles for $Sr_{1.31}Co_{0.63}Mn_{0.37}O_3$. The black vertical ticks stand for the reflection positions.

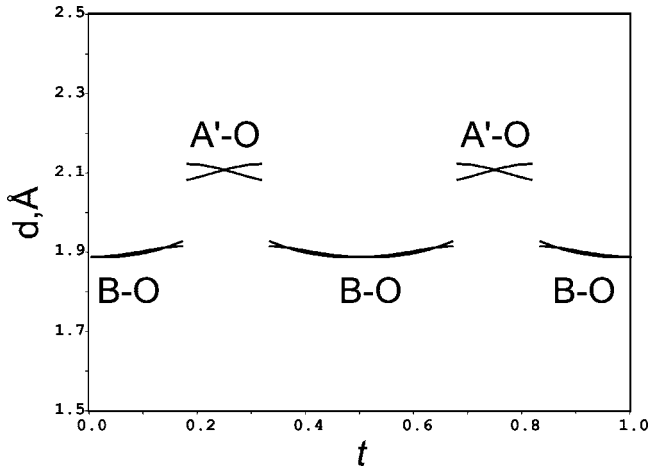

Figure 5. A′–O and B–O distances versus t for $Sr_{1.31}Co_{0.63}Mn_{0.37}O_3$.

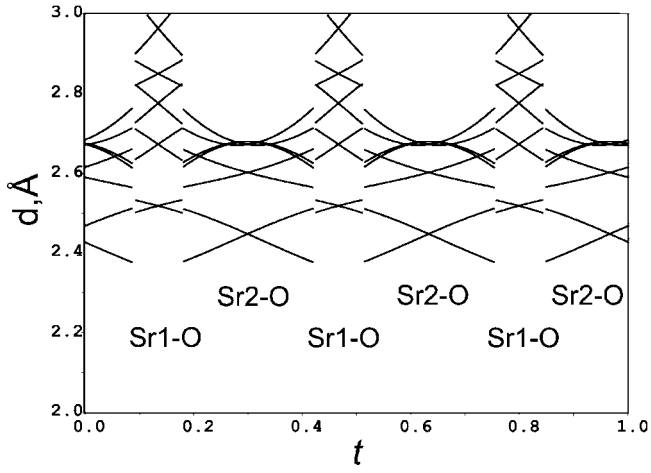

Figure 6. Sr1–O and Sr2–O distances versus t for $Sr_{1.31}Co_{0.63}Mn_{0.37}O_3$.

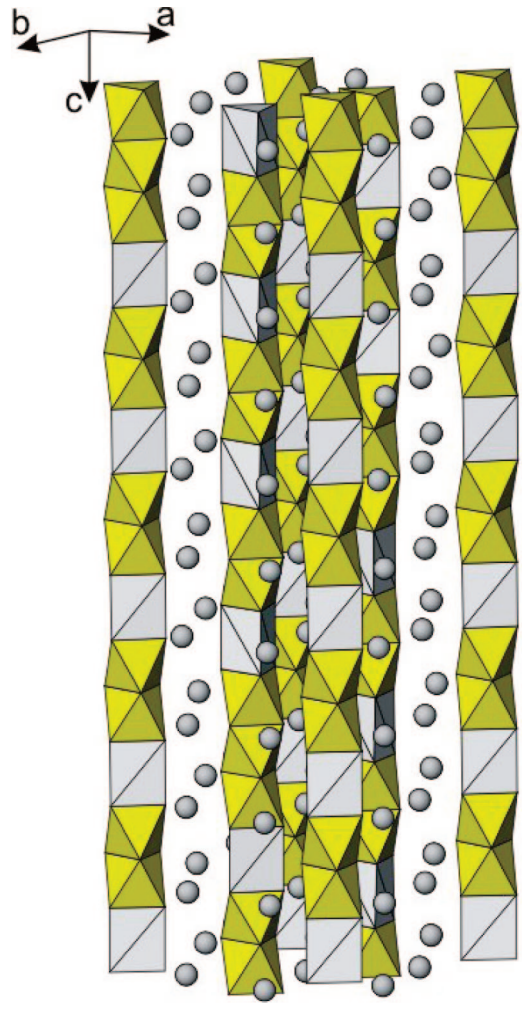

Figure 7. Structure of the commensurate $x = 5/16$ ($\gamma = 21/32$) approximant. One half of the unit cell along the c-axis is shown.

Nevertheless, we wish to report the detailed pre-edge results to motivate future theoretical modeling of the pre-edge region.

In Figure 11a,b we present the Mn and Co–K pre-edges for $Sr_{1.31}Co_{0.63}Mn_{0.37}O_3$ along with those for the various standard compounds noted above. The prominent a1–a2 feature (see

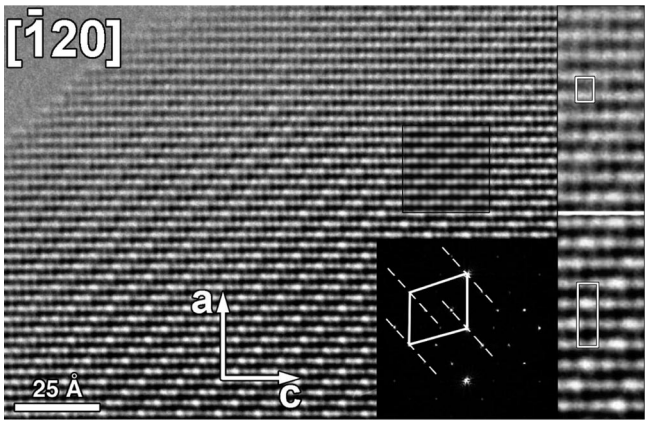

Figure 8. High-resolution [1̄20] electron microscopy image of $Sr_{1.3}Co_{0.64}Mn_{0.36}O_3$ citrate sample. The calculated image is shown as an square inset in the right part. The Fourier transform of the image is shown in the bottom left corner. The solid and dashed lines on the Fourier transform indicate the primitive part of the rhombohedral unit cell of the subsystem I and the direction of satellite arrays, respectively. On the enlarged part of the image at the right side the unit cells of both subsystems are shown in real space (top rectangle (thin area): primitive unit cell of the subsystem II; bottom rectangle (thicker area): rhombohedral unit cell of the subsystem I).

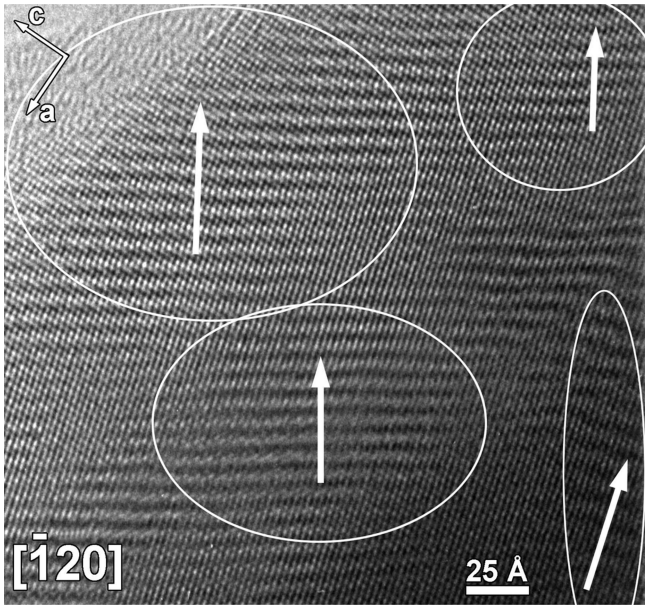

Figure 9. Overview image of the $Sr_{1.3}Co_{0.64}Mn_{0.36}O_3$ ceramic sample along [1̄20] showing the coexistence of domains with different γ component of the modulation vector. White arrows correspond to the direction of the normal to the diagonal dark stripes indicating the modulation and are seen to differ in orientation from area to area.

Figure 11a) in the Mn pre-edge spectrum of $Sr_{1.31}Co_{0.63}Mn_{0.37}O_3$ (despite the mixed local symmetries) does show a similarity in spectral aspects to those of the $CaMn^{4+}O_3$ standard. This supports the Mn^{4+} valence state assignment from the main edge results above. The much greater relative intensity of the a1 feature in the $Sr_{1.31}Co_{0.63}Mn_{0.37}O_3$ pre-edge (relative to the $CaMn^{4+}O_3$ standard) could be caused by an enhancement of p-hybridization due to noncentrosymmetric local environments; arguably a trigonal prismatic-related feature could contribute in the a1 region. However, since each octahedral site is bounded on one face to a trigonal prism and on the opposite face to an octahedron, the octahedral sites also lack strict centrosymmetry. These interpretations must however be regarded as tentative.

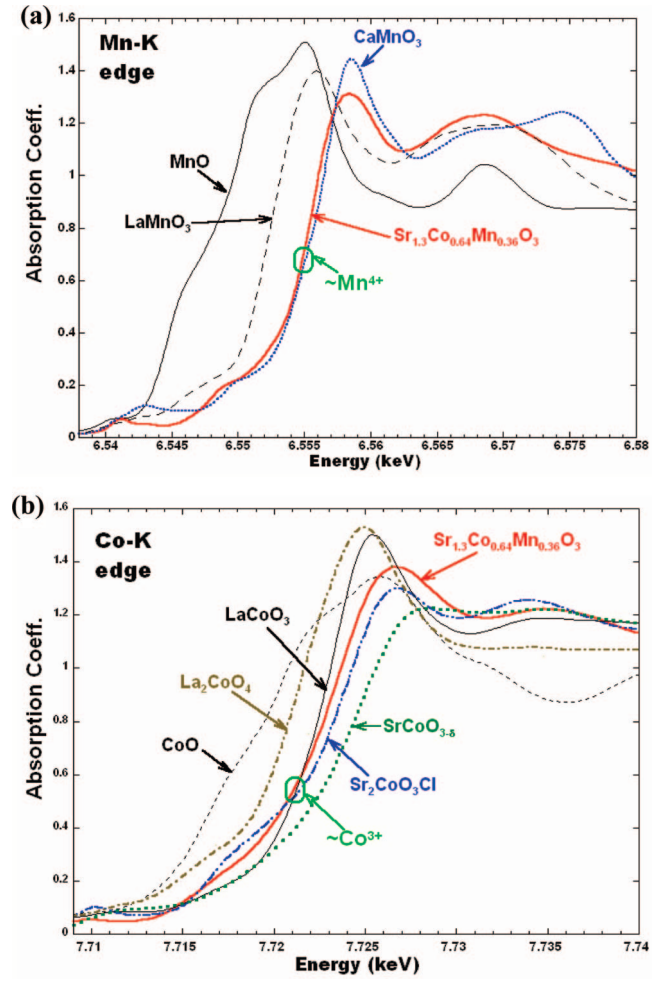

Figure 10. Main edge XAS spectra at the (a) Mn–K and (b) Co–K edges of $Sr_{1.31}Co_{0.63}Mn_{0.37}O_3$ along with a number of standard compounds.

In the case of the Co–K pre-edges shown in Figure 11b, the $Sr_{1.31}Co_{0.63}Mn_{0.37}O_3$ spectrum manifests a distinctly different shape, a single intense feature, compared to the octahedral Co standards. The $Sr_2Co^{3+}O_3Cl$ material, with its apical Cl substitution breaking the local symmetry, also manifests a similar, albeit much stronger, feature. In this case the local symmetry disparity appears to dominate the pre-edge spectra, making clear observations regarding the Co valence impossible. Recent studies[44] have shown a similar transition from a more typical bimodal pre-edge for Na_1CoO_2 to a single feature for Na_xCoO_2 ($x < 0.8$) materials. The strength and structure of the Co pre-edge presumably are determined by the nature of noncentrosymmetry. Investigation of Co materials with a trigonal-prismatic local structure is clearly called for before realistic conclusions on the pre-edge features in $Sr_{1.31}Co_{0.63}Mn_{0.37}O_3$ can be made.

3.5. Magnetic Properties. Considering the structural complexity and inherent disorder present in the $Sr_{1.31}Co_{0.63}Mn_{0.37}O_3$ system, interpretation of the bulk magnetic data is problematic at best. The temperature dependence of

(44) Poltavets, V. V.; Croft, M.; Greenblatt, M. *Phys. Rev. B* **2006**, *74*, 125103.

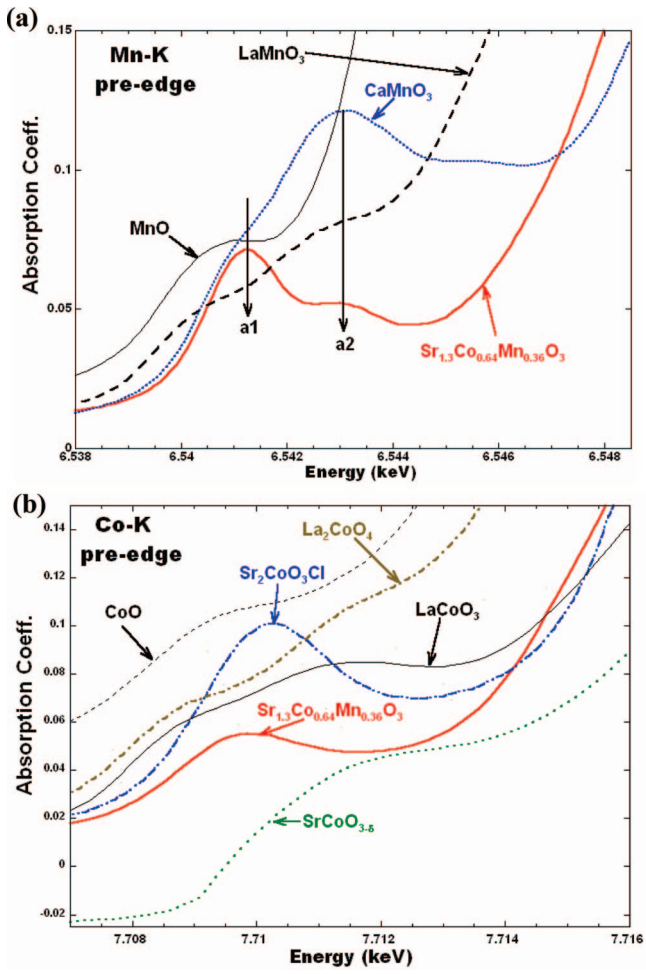

Figure 11. Pre-edge XAS spectra at (a) Mn–K and (b) Co–K pre-edges of $Sr_{1.31}Co_{0.63}Mn_{0.37}O_3$ along with a number of standard compounds.

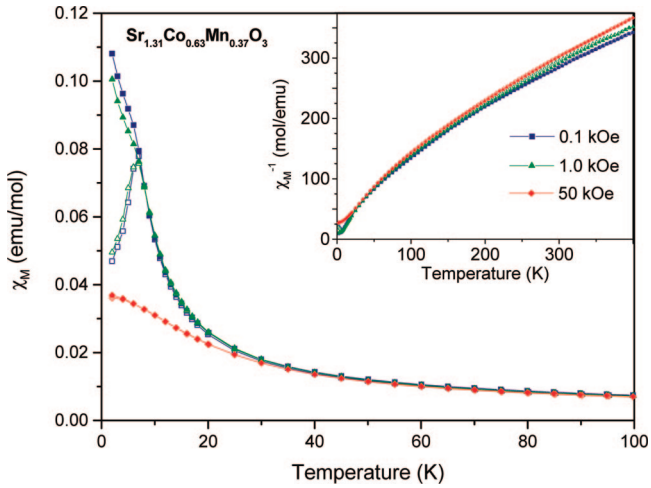

Figure 12. Temperature dependence of the molar magnetic susceptibility of $Sr_{1.31}Co_{0.63}Mn_{0.37}O_3$ in the temperature range 2–100 K. Inset shows the temperature dependence of the inverse molar susceptibility.

magnetic susceptibility (both FC and ZFC) data at different applied fields for $Sr_{1.31}Co_{0.63}Mn_{0.37}O_3$ is shown in Figure 12. The FC and ZFC data measured at a static field of 100 and 1000 Oe coincide down to 7 K, below which they deviate. Since no evidence for long-range order was observed in the neutron scattering results at 5 K, the peak in the ZFC susceptibility at ~7 K is presumably related

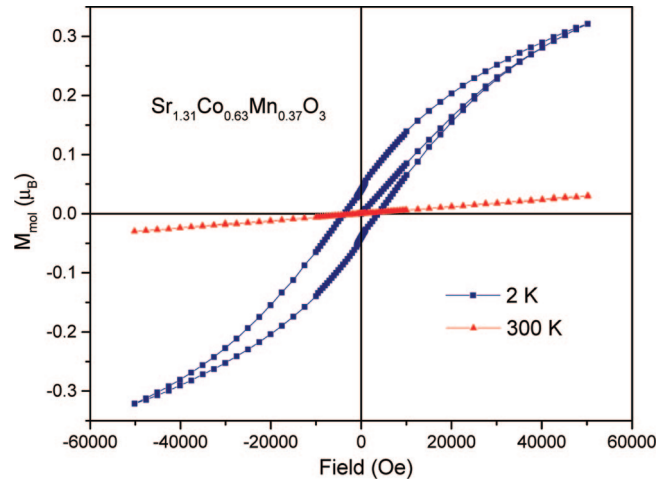

Figure 13. Field dependence of magnetization data for $Sr_{1.31}Co_{0.63}Mn_{0.37}O_3$ at 2 and 300 K.

to concentrated spin glass/mictomagnetic[45] freezing. Indeed, the irreversibility of the magnetization curves at 2 K (Figure 13) also supports magnetic glassy behavior.

The inverse susceptibility versus temperature (inset of Figure 12) clearly manifests curvature at all temperatures, making any Curie–Weiss (CW) law fit subjective. Performing a CW fit to the 1000 Oe data in the temperature range 300–400 K yields a θ of ~ -195 K. This could be interpreted as indicative of antiferromagnetic (AF) short-range correlations. Since many of the spins will be unequal in magnitude, such correlations would in fact be ferromagnetic-like. The Curie constant for this high temperature CW fit is $C = 1.689$ emu K mol^{-1} and yielding an effective paramagnetic moment, $\mu_{\text{eff}} = 3.676\ \mu_B$. A calculation of the effective magnetic moment ($\mu_{\text{cal}} = 3.561\ \mu_B$) is obtained with a series of assumptions: Co^{3+} and Mn^{4+} formal oxidation states, as indicated by the XAS results; the cation distribution from the NPD refinement; a low-spin (LS) $S = 0$ state for the octahedral $Co_{oct}{}^{3+}(d^6)$ sites; a high-spin (HS) $S = 2$ state for the trigonal prismatic $Co_{tp}{}^{3+}(d^6)$ sites; and finally a $S = {}^3/_2$ configuration for the $Mn_{oct/tp}{}^{4+}(d^3)$. Under these assumptions (and recalling the continuous curvature of the inverse susceptibility) the theoretical and experimental moment values are in fairly good agreement.

In view of the curvature of the inverse susceptibility, one can also fit the low-temperature data to a CW-like tail and then subtracting this tail to form the "corrected" high-temperature susceptibility. Doing so produces a maximum in the "corrected" susceptibility which can vary from 100 to 400 K depending on the detailed region of fit of the CW tail. Whether this is due to AF correlations or an excited higher spin state[46] on octahedral Co^{3+} sites is unclear.

4. Conclusions

In conclusion, we have extended the series of the $Sr_{1+x}Co_yMn_{1-y}O_3$ compounds toward the composition with

(45) Mydosh, J. A. *Spin glasses: An Experimental Introduction*; Taylor & Francis: London, 1993.
(46) Raccah, P. M.; Goodenough, J. B. *Phys. Rev.* **1967**, *155*, 932.

Co/Mn $\approx$ 2 ratio. We have carried out the detailed structural, microstructural, and magnetic characterization of $Sr_{1.31}Co_{0.63}Mn_{0.37}O_3$ with a combination of PXD, NPD, EDX, ED, HREM, XAS, and magnetic susceptibility studies. $Sr_{1.31}Co_{0.63}Mn_{0.37}O_3$ adopts an incommensurately modulated composite structure related to the 2H hexagonal perovskite containing chains of face-sharing octahedra and trigonal prisms. Because of chemical inhomogeneity, the complex microstructure was observed consisting of domains with slightly different lengths of the modulation vector as evidenced by HREM studies. The presence of Mn^{4+} and Co^{3+} cations in our system was evidenced by XAS measurements. The NPD data indicate that the Co^{3+} ions preferentially occupy the trigonal-prismatic site, while the octahedral site is filled with Mn^{4+} and Co^{3+} in nearly equal amounts. Considering the structural and microstructural complexity and inherent disorder present in this compound, a definitive interpretation and modeling of the bulk magnetic data would require further research with single crystals.

Acknowledgment. We acknowledge the support of the National Institute of Standards and Technology (NIST), U.S. Department of Commerce, in providing the neutron research facilities used in this work. T.K.M. and M.G. thank Dr. Judith K. Stalick for her help with the neutron data collection at BT-1, NCNR. T.K.M. thanks Viktor Poltavets and Guerman Popov for their help with the magnetic measurements. This work was supported by the National Science Foundation through NSF-DMR-0233697, NSF-DMR-0541911 (T.K.M., M.G.), and RFBR grants 07-03-00664-a, 06-03-90168-a, and 05-03-34812-MF-a.

CM071840G